Journal of Dynamics, Monitoring and Diagnostics, 2026, 5, 86-95
https://doi.org/10.37965/jdmd.2026.1166

ISTP
RESEARCH ARTICLE

Noise–Vibration Monitoring and Analysis of Aero-Engine Blade Fracture Faults

Minghui Hu,[1,2] Xiaoyang Zhang,[1,3] Tao Zhou,[1,2] and Baoteng Jin[1,3]

[1]State Key Laboratory of High-end Compressor and System Technology, Beijing University of Chemical Technology, Beijing 100029, China

[2]Beijing Key Laboratory of Health Monitoring and Self-Recovery for High-End Mechanical Equipment, Beijing University of Chemical Technology, Beijing 100029, China

[3]Key Lab of Engine Health Monitoring-Control and Networking of Ministry of Education, Beijing University of Chemical Technology, Beijing 100029, China

(Received 30 January 2026; Revised 16 March 2026; Accepted 16 March 2026; Published online 17 March 2026)

Abstract: This study investigates the vibration and noise response characteristics of faulty blades through mechanistic modeling and validates the established model via full-scale engine tests. In the modeling stage, based on the physical mechanism of wake-induced aerodynamic excitation acting on blades, the dynamic characteristics of the aerodynamic force acting on the first-stage high-pressure blade are analyzed. A stator blade model is developed, incorporating aerodynamic dynamic pressure theory, a Rayleigh damping formulation, and a fourth-order finite-difference approximation to describe the blade bending stiffness. The governing equations are discretized using the finite-difference method, and the blade response under aerodynamic excitation is solved using the Newmark-β method; this process establishes the coupling relationship between aerodynamic excitation and system dynamic response. The numerical results indicate that blade fracture leads to a pronounced amplification of the rotor shaft rotational frequency component, while the amplitudes of the blade passing frequency (BPF) and its harmonics are significantly attenuated. Further, full-scale engine tests were designed and carried out under three operating conditions for both healthy and fractured blades. Signal processing results demonstrate that the extracted fault features are in good agreement with the predicted system dynamic response, therefore, the experimental results confirm the accuracy and validity of the proposed model. The conclusions of this study provide a reliable theoretical reference and quantitative benchmark for identifying the response characteristics of blade fracture faults in aero-engines, providing practical engineering value for the fault diagnosis and health monitoring of blades.

Keywords: aero-engines; blade fracture; Euler–Bernoulli beam model; full-scale engine tests; noise signal analysis; vibration signal analysis

I. INTRODUCTION

Aero-engine blades are critical load-bearing components for energy conversion and power output, whose structural integrity directly affects the safety and operational reliability of the engine. However, under the combined effects of frequent start-ups, acceleration/deceleration cycles, and alternating complex operating conditions, blades are subjected to long-term multisource coupled loads, making them highly prone to damage or even fracture. Once blade failure occurs, it often triggers severe secondary damage and may even lead to catastrophic engine accidents.

Extensive research has been conducted on the response characteristics of blade fracture faults from both simulation modeling and experimental simulation perspectives, yielding fruitful results. Yang *et al.* [1] developed a general analytical modeling approach for rotor blade cracks that introduces a crack-interface stress-state criterion. This systematically addresses the limitations of traditional displacement-based models in characterizing the nonlinearities of high-speed rotor blades with cracks. Yang *et al.* [2] established a coupled dynamic model of the bladed disk rotor system. By systematically analyzing the interaction characteristics among the various components, the study theoretically elucidated the coupled vibration mechanisms of the system, providing effective support for the vibration monitoring and fault diagnosis of rotor blades. Feng *et al.* [3] developed a gas turbine blade condition monitoring method based on broadband casing vibration, using Sparse Harmonic Product Spectrum (SHPS), adaptive Vold–Kalman filtering, and unsupervised learning to estimate blade passing frequency (BPF), extract blade-related vibration, and achieve early fault detection and localization. Pedro *et al.* [4] presented an ideal blade sweep model, applied a modified Blade Element Momentum (BEM) code, and simulated 20-kW HAWTs with straight, exponential, and ideal swept blades. Ibrahim *et al.* [5] focused on the theoretical study of sudden unbalance and rub-impact phenomena caused by blade loss, analyzing the effects of blade number, speed ratio, disk eccentricity, and friction stiffness on the casing acceleration response. Chuang *et al.* [6] proposed an enhanced reduced order model (EROM) and EROM-DMID method for aero-engine rotating bladed disks. Amanda *et al.* [7] investigated blade loads of a model tidal turbine under unsteady gust forcing. They evaluated 2D strip-theory validity by comparing with 3D RANS/VLM simulations. Bingbing *et al.* [8] studied nonlinear vibration and vibration reduction of integrally shrouded group blades and proposed a lumped parameter model. Zhang *et al.* [9] proposed an early weak fault

Corresponding author: Minghui Hu (e-mail: humh2008@163.com).

identification method for micro-turbine blades based on sound pressure signals and long short-term memory (LSTM) networks. By combining spectral analysis with wavelet packet energy feature extraction, the approach enables effective detection and identification of early blade faults and has been experimentally validated under multiple operating conditions. Chidambaram *et al.* [10] conducted a systematic engineering failure analysis and material characterization test on the fracture accident of the last-stage blade of a 600 MW power plant low-pressure steam turbine. Weijian *et al.* [11] proposed a method for precisely controlling the blade fracture speed through prefabricated cracks to address the high risk and uncertainty in turbofan engine blade loss containment tests. Daitong *et al.* [12] proposed a novel online vibration measurement method based on blade tip pulse width (BTPW), analyzing the vibration amplitude, resonance frequency, and mistuning characteristics of rotating blades and blisks through simulation and actual engine test data. Du J. *et al.* [13] proposed an aero-engine full-engine jet noise localization and identification method based on the Clean-SC sound source imaging technology and a linear microphone array. Anil [14] reviewed commonly used condition monitoring techniques for compressors and highlighted recent advances in feature extraction, dynamic modeling, and AI-based predictive maintenance. The study also discussed industrial applications, identified key challenges and research gaps, and proposed a continuous learning and model adaptation framework for real-time performance improvement. Hou *et al.* [15] investigated acoustic emission (AE) responses of wind turbine blades under controlled fatigue loading with staged crack propagation in different structural regions. By combining spatiotemporal filtering, feature extraction, and unsupervised clustering, the work revealed region-dependent AE characteristics and demonstrated that AE signals can effectively capture localized crack initiation and propagation processes, providing a region-aware framework for structural health monitoring of large blades. Zhao *et al.* [16] studied a multistage high-pressure compressor and showed that strong rotor blade vibration is closely coupled with discrete multitone noise generated by acoustic resonance. The characteristic acoustic frequency remains locked within a specific speed range and is modulated by rotor speed, forming a helical propagation pattern in the compressor. The results indicate that acoustic resonance and its sideband components can act as an important excitation source of rotor blade vibration and should be considered in blade fault analysis. Rafiee *et al.* [17] summarized beam theories for rotating composite beams and blades, followed by a comprehensive overview of analytical, semi-analytical, and numerical methods. Adaptive and smart rotating composite beams, along with damping and vibration control strategies, are discussed. The application of advanced materials such as functionally graded materials and nanocomposites is examined. Complicating factors—including tip mass, nonuniform cross-section, initial curvature or twist, swept tip, and size-dependent effects—are analyzed in terms of their influence on dynamics and vibration reduction. Shen *et al.* [18] derived a recursive solution to the nonlinear vibration equation of cracked blades, revealing the quantitative relationship between harmonic power and crack parameters and establishing the upper bound of adjacent harmonic power ratios. Harmonic power decreases with order, governed by crack characteristics. A crack detection method based on harmonic power ratios is proposed, applicable over the full speed range without resonance. Simulations and noncontact experiments validate its effectiveness. Wang *et al.* [19] investigated acoustic resonance in an aero-engine compressor through forced surge tests on a 3.5-stage compressor, with synchronized acquisition of unsteady pressure, blade vibration, and acoustic signals. The results indicate that acoustic resonance is governed by spatial mode coupling and phase locking rather than sequential excitation. Axial analysis shows that resonant energy originates in the cavity between the inlet guide vane and the first-stage rotor and attenuates downstream. Pradeep Kundu [20] reviewed AE-based condition monitoring for rotating machinery. It summarizes AE signal characteristics, the influence of operating parameters, and standard practices for data measurement and analysis. Compared with vibration signals, AE detects high-frequency transient elastic waves and is less affected by mechanical resonance and background noise, enabling the capture of broadband defect information beyond the vibration sensor's range. AE is more sensitive to incipient faults, as small surface defects may not alter structural vibration but significantly affect AE activity. Moreover, AE sources radiate spherically, allowing flexible sensor placement and fault source localization. Wu *et al.* [21] proposed an axial-bending coupled breathing crack model based on Timoshenko beam theory and Castigliano's principle to investigate the vibration characteristics of cracked rotating blades, which was validated by FEM simulations and experiments. The results showed that crack-induced axial-bending coupling significantly affects blade vibration responses, and the axial response is more sensitive to crack nonlinearity, providing useful indicators for crack detection and severity evaluation. Hou *et al.* [22] conducted a full-scale aero-engine experiment with inter-shaft bearing faults and proposed a vibration-based fault dataset derived from rotor and casing signals. Artificial bearing faults were introduced on a real aero-engine test rig, and vibration signals were collected under multiple high- and low-pressure rotor speed conditions using displacement and acceleration sensors. Based on this dataset, fault diagnosis was performed using spectrum analysis, envelope analysis, and deep learning models including CNN, LSTM, and TST, and the results were compared with the CWRU and XJTU datasets. Wu *et al.* [23] proposed a cracked bladed-disk coupling model considering a flexible disk and elastic boundary support to address the limitations of conventional rigid-disk assumptions. The model was developed based on Kirchhoff plate theory and Timoshenko beam theory, where crack-induced stiffness loss was calculated using released strain energy, and the elastic support at the disk inner edge was simulated by linear and torsional springs. The model was validated through FEM and experiments, and the effects of crack depth and location on the coupling vibration characteristics were investigated. Wu *et al.* [24] developed a dynamic model of a flexible dual-rotor system to investigate the influence of blade cracks on the modal characteristics of the coupled system. The model was established using a finite element–assumed modes (FE–AM) hybrid method, where crack-induced stiffness loss was calculated based on released strain energy and validated through FEM and experiments. The results showed that blade cracks can induce mode localization and mistuned distributions and lead to coupling between blade bending and shaft torsional modes. Wu *et al.* [25] developed a shaft–disk–cracked blade coupled dynamic model to investigate the vibration characteristics of cracked blades under multisource excitations, including gravity, unbalance, and aerodynamic loads. The model was established using an FE–AM hybrid approach and validated by comparison with FEM and existing literature. The results show that blade cracks cause equilibrium offsets in

blade tip bending displacement and induce additional torsional vibrations in the shaft, while the amplitude ratios of blade bending and shaft torsion can serve as effective indicators for evaluating breathing cracks.

As evident from the above, vibration-based condition monitoring is the primary technical means for aero-engine fault diagnosis. However, under the background of strong aerodynamic excitation and multisource vibration coupling, vibration features caused by local blade damage are often masked by background vibration and overall system response. Particularly in the early stage of local fracture, the amplitude of vibration feature changes is limited, resulting in constrained monitoring sensitivity and robustness. In contrast, noise signals are not subject to such interference, as they can detect high-frequency elastic stress waves generated by blade fracture, which can directly reflect local damage characteristics.

Noise monitoring technology, as a nonintrusive, real-time, and low-cost fault diagnosis method, can overcome the shortcomings of traditional vibration sensors. In terms of sensor deployment, noise sensors can be placed anywhere near the signal source, and signal collection from a single direction is sufficient to obtain effective fault information. In contrast, vibration sensors typically require data collection from three axes to comprehensively capture the dynamic response of the system, which increases the complexity of monitoring systems and deployment costs. Therefore, by combining noise and vibration signals to jointly analyze the fault characteristics related to aero-engine blade fracture, more accurate conclusions can be drawn.

Based on this, this study investigates the vibration and noise response characteristics of aero-engine blade fracture faults through a combination of simulation modeling and full-engine experiments. The main innovations are as follows:

(1) A coupled blade dynamic model integrating structural dynamics and wake excitation force is constructed to simulate blade fracture faults from a mechanistic perspective, thereby revealing the influence of faults on system response characteristics.

(2) A mapping relationship between fault severity and signal features is established. The occurrence of blade fracture faults is characterized by changes in the amplitudes of frequency components such as shaft rotational frequency and BPF, and the quantitative correlation between them is clarified.

(3) Full-engine-level blade fracture simulation tests are conducted, with synchronous collection of multisource vibration and noise signals. The accuracy of simulation conclusions is verified by comparing shaft rotational frequency and BPF obtained from experiments with the predictions of the dynamic model.

II. MODEL CONSTRUCTION

A. ACTION MECHANISM OF WAKE EXCITATION FORCE ON BLADES

Wake excitation force is the primary form of aerodynamic excitation for aero-engine blades, originating from airflow pulsation in the flow channel. Upstream blades periodically block and separate the airflow, forming a wake structure propagating with the flow. When downstream blades periodically sweep through this wake field, the aerodynamic force on their surfaces fluctuates periodically with the arrival and departure of the wake, generating wake excitation force. Figure 1 illustrates the formation of wake excitation force on blades.

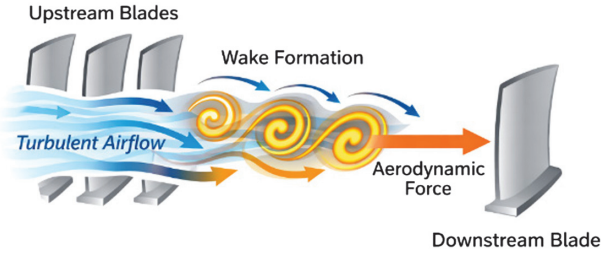

Fig. 1. Effect diagram of airflow excitation force on the blades.

The core characteristics of this excitation force are frequency determinism and amplitude pulsation: the frequency is jointly determined by the rotor rotational speed n and the number of upstream blades Z, the BPF:

$$BPF = n \cdot Z/60 \tag{1}$$

Its amplitude is related to aerodynamic dynamic pressure, wake intensity, and other factors.

B. ESTABLISHMENT OF ONE-DIMENSIONAL EULER–BERNOULLI CANTILEVER BEAM MODEL

In this study, stator blades are simplified as Euler–Bernoulli one-dimensional cantilever beam models. Blade fracture is simulated by modifying the wake excitation force load caused by upstream rotor blade damage. Figure 2 shows the mechanical schematic of the beam model under aerodynamic excitation.

The dynamic control equation of the cantilever beam is

$$\rho A \frac{\partial^2 y}{\partial t^2} + c\frac{\partial y}{\partial t} + EI\frac{\partial^4 y}{\partial x^4} = p(x,t) \tag{2}$$

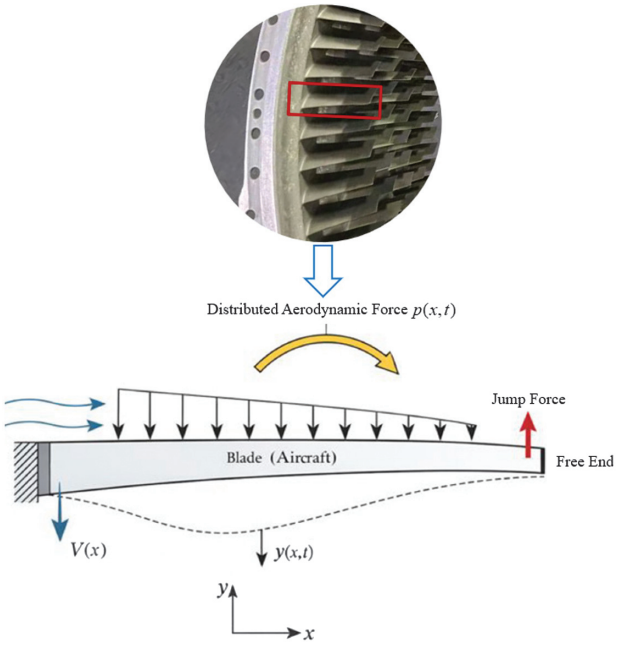

Fig. 2. The real blade is simplified into an Euler-Bernoulli one-dimensional cantilever model.

where y is the displacement function, $p(x,t)$ is the distributed load, ρ is the mass density, A is the cross-sectional area, c is the equivalent damping coefficient, and EI is the flexural stiffness. $\rho A\frac{\partial^2 y}{\partial t^2}$ represents the inertial force per unit length, reflecting the inertial response of the beam element to acceleration, $c\frac{\partial y}{\partial t}$ represents the viscous damping force per unit length, describing the energy dissipation due to the damping effect, $EI\frac{\partial^4 y}{\partial x^4}$ represents the flexural restoring force per unit length, which is derived from the internal bending moment and reflects the beam's resistance to bending deformation, and $p(x,t)$ represents the distributed aerodynamic excitation force acting on the beam.

The equation for the uniformly distributed aerodynamic exciting force under steady-state conditions is

$$p(x,t) = \frac{1}{2}\rho_{air} C_L A_{proj} v^2(t) \tag{3}$$

where C_L is the aerodynamic coefficient, comprehensively considering the influence of aerodynamic shape and angle of attack, A_{proj} is the windward projected area, and v is the airflow velocity.

The specific modeling steps are as follows:

(1) Define the geometric and material parameters of the cantilever beam: equivalent cross-sectional dimensions b (width) and h (thickness); elastic modulus E; moment of inertia of the cross-section I; material density ρ; and cross-sectional area A, where

$$A = b \cdot h \tag{4}$$

$$I = \frac{b \cdot h^3}{12} \tag{5}$$

(2) Introduce a periodic wake excitation model based on the BPF, representing the periodic sweeping of downstream blades by the wake of upstream blades, forming the main excitation at BPF, which is one of the dominant excitation sources for turbine blades.

The aerodynamic excitation is decomposed into a steady component and a periodic perturbation induced by rotor–stator interaction at the BPF. Its time-varying aerodynamic force model is

$$P(t) = p + \Delta p \sin(\omega_{BPF} t) \tag{6}$$

$$\omega_{BPF} = 2\pi \cdot N_s \cdot N_b \tag{7}$$

where ω_{BPF} is the main excitation frequency determined by the rotor rotational speed N_s and the number of blades N_b, when the rotor speed N_s is given in revolutions per second (*rps*), the sine term simulates the periodic aerodynamic pulsation caused by wake and rotor–stator interaction, and Δp is the amplitude of aerodynamic pulsation.

It should be clarified that the uniformly distributed aerodynamic load $p(x,t)$ given in Eq. (3) represents the steady-state mean aerodynamic force under constant inflow conditions and serves as the baseline component of the excitation model. When rotor–stator interaction and wake sweeping effects are considered, this steady component is retained as the constant term in the time-varying formulation. Accordingly, the constant term p in Eq. (6) is directly derived from Eq. (3), while Δp represents the amplitude of the periodic aerodynamic pulsation at the BPF. When blade fracture occurs, the effective load-bearing area decreases and the local flow structure changes, resulting in a reduction of Δp and thus a decrease in pulsation amplitude.

Fracture leads to a decrease in the fluctuation amplitude, and the wake-induced periodic disturbance can be expressed as:

$$\Delta p_f = \eta_f \cdot \Delta p_n \tag{8}$$

where $\eta_f \in (0,1)$ is the fracture attenuation coefficient. Normal load Δp_n: uniform pressure superimposed with periodic wake pulsation. Fault load Δp_f: when the blade fractures, the pulsation amplitude decreases, where $\eta_f \in (0,1)$ is the fracture attenuation coefficient, and the load amplitude is dynamically adjusted according to the number of fractured blades.

Accordingly, the aerodynamic load under fault condition becomes

$$P_f(t) = p + \eta_f \Delta p_n \sin(\omega_{BPF} t) \tag{9}$$

where η_f reflects the severity of the blade fracture and can be adjusted according to the number of fractured blades.

(3) Discretization using the finite-difference method: The cantilever beam is discretized into N_x nodes to generate a uniform grid with a node spacing of Δ_x. The continuous beam is converted into a multi-degree-of-freedom system through discretization to facilitate numerical calculation. The spatial discretization form is

$$\mathbf{M}\ddot{u} + \mathbf{K}u = P(t) \tag{10}$$

where $\mathbf{M}$ is the mass matrix and $\mathbf{K}$ is the stiffness matrix.

(4) Construction of mass matrix and stiffness matrix:

Mass matrix $\mathbf{M}$:

$$\mathbf{M} = \rho A \cdot \Delta x \cdot I \tag{11}$$

Based on the lumped mass method, the diagonal elements are $\rho A\Delta_x$ representing the node mass.

Stiffness matrix $\mathbf{K}$: (second-order central difference + cantilever boundary conditions)

$$\mathbf{K} = \frac{EI}{\Delta x^4}\mathbf{K_{FD}} \tag{12}$$

where $\mathbf{K_{FD}}$ is the finite-difference stiffness operator matrix. The bending stiffness of the beam is approximated based on the fourth-order derivative difference format, reflecting the elastic coupling relationship between nodes.

(5) Boundary condition processing: The left end is fixed, and the right end is free. By setting the first row and first column of $\mathbf{K}$ and $\mathbf{M}$ to $\mathbf{0}$, and setting the diagonal element of the first row to $\mathbf{1}$, the displacement and rotation angle at the fixed end are forced to $\mathbf{0}$.

(6) The Rayleigh damping model is used to reflect the structural energy dissipation and noise amplitude control mechanism, enabling the alignment of simulation response amplitude with test amplitude. The damping matrix $\mathbf{D}$ can be calculated through the damping ratios at two frequency points: mass-proportional damping is dominated by low frequencies, and stiffness-proportional damping is dominated by high frequencies.

The specific calculation formula is

$$\mathbf{D} = \alpha\mathbf{M} + \beta\mathbf{K} \tag{13}$$

where $\alpha = \frac{2\zeta_1\omega_1\zeta_2\omega_2}{(\zeta_2\omega_2 - \zeta_1\omega_1)}, \beta = \frac{(\zeta_1\omega_2 - \zeta_2\omega_1)}{(\zeta_2\omega_2 - \zeta_1\omega_1)}$, and α and β are determined using two target modal damping ratios (ζ_1,ζ_2). ω_1 and ω_2 are the damping ratios at frequencies.

(7) Numerical solution method: The Newmark-β method (implicit time integration) combined with the Rayleigh damping model is used to solve the real-time domain vibration response of the blade under aerodynamic excitation. The dynamic equation is solved to calculate the displacement, velocity, and acceleration time histories:

$$\mathbf{M}\ddot{u}(t) + \mathbf{D}\dot{u}(t) + \mathbf{K}u(t) = P(t) \tag{14}$$

where $\boldsymbol{\beta} = \mathbf{0.25}$ and $\boldsymbol{\gamma} = \mathbf{0.5}$ are adopted for unconditional stability.

C. SIMULATION RESULT ANALYSIS

Based on the blade model and the wake-induced excitation model established in the previous chapter, this chapter investigates the dynamic response characteristics of blades under fracture fault conditions through numerical simulations.

To facilitate reproducibility and comparison, the geometric parameters and material properties used in the blade model are summarized as follows. The blade is modeled as a cantilever beam with a length $L = 1.0\,\mathrm{m}$. The material is assumed to be steel with a Young's modulus $E = 2.1 \times 10^{11}$ Pa and a density $\rho = 7800\,\mathrm{kg/m^3}$. The cross-sectional area of the blade is $A = 1.0 \times 10^{-4}\,\mathrm{m^2}$, and the area moment of inertia is $I = 1.0 \times 10^{-6}\,\mathrm{m^4}$. These parameters are used in the dynamic modeling and numerical simulation of the blade vibration response.

To ensure the physical rationality of the aerodynamic load model, the parameters in Eq. (3) are selected according to the typical aerodynamic conditions of aero-engine compressor blades. The air density ρ_{air} is generally in the range of **1.1–1.3 kg/m^3** under standard atmospheric conditions, and a value of **1.225 kg/m^3** is adopted in this study. The aerodynamic lift coefficient C_L of compressor blades typically varies between **0.8** and **1.2** depending on blade geometry and angle of attack; therefore, $C_L = 1.0$ is used as a representative value. The airflow velocity in compressor flow passages is usually within **200–300 m/s**, and $v = 250\,\mathrm{m/s}$ is selected in the present model. The equivalent windward projected area is approximately $A_{proj} \approx 1.05\,\mathrm{m^2}$.

Substituting the parameters into Eq. (3) yields the uniformly distributed aerodynamic load $p = 40000$ N/m used in the numerical simulations; the pressure pulsation amplitude caused by the wake under normal conditions $\Delta p = 20000$ N/m; the pressure pulsation amplitude caused by the wake under fracture conditions $\Delta p = 16000$ N/m; shaft rotational frequency = 10 Hz; number of blades $n = 10$; BPF = 100 Hz. The sixth-stage blade is fractured, and then the aero-engine blade fracture fault can be simulated by changing the magnitude of the excitation force. Under normal conditions, the vibration response waveform is obtained as shown in Fig. 3(a), and the spectrogram is obtained through fast Fourier transform (FFT) as shown in Fig. 3(b). Under fault conditions, the vibration response waveform is obtained as shown in Fig. 4(a), and the spectrogram is obtained through FFT as shown in Fig. 4(b).

The time-domain response under blade fracture conditions is illustrated in Fig. 4(a). With a shaft rotational frequency of 10 Hz, the duration of one complete rotation

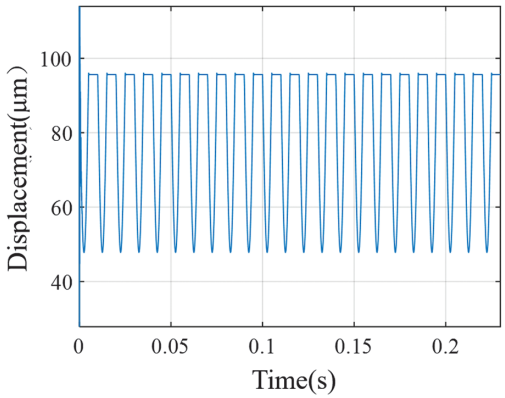

(a) Time-domain waveform

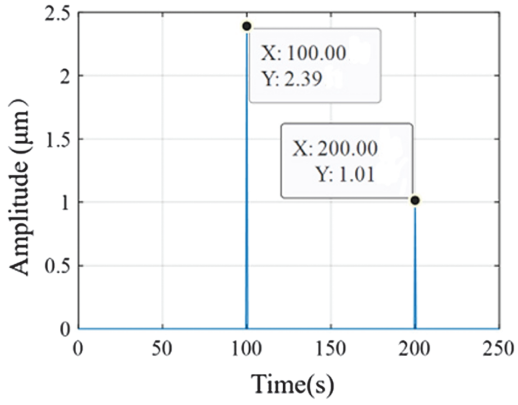

(b) Spectrogram

Fig. 3. Simplified cantilever beam model response under healthy blade conditions. (a) Time-domain waveform. (b) Spectrogram.

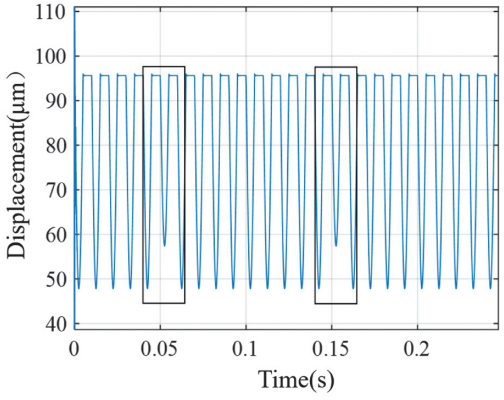

(a) Time-domain waveform

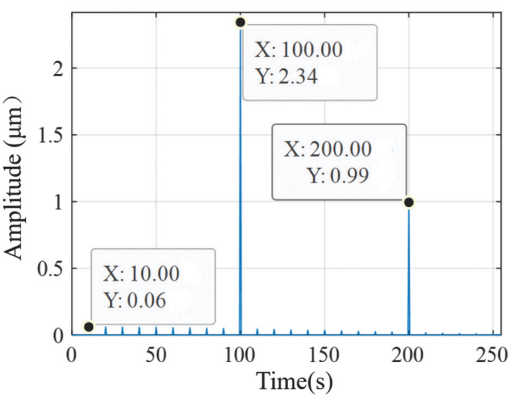

(b) Spectrogram

Fig. 4. Response of a simplified cantilever beam under blade fracture failure. (a) Time-domain waveform. (b) Spectrogram.

is 0.1 s. Given that it consists of $n = 10$ blades, there are 10 distinct pressure pulsations occurring within each 0.1 s interval. Since the sixth-stage blade is simulated with a fracture fault, as shown in the waveform, every sixth pulse within the rotational period displays a significantly lower displacement amplitude compared to the others. This periodic variation accurately reflects the fault of the sixth blade, as the reduced excitation force Δp leads to a localized decrease in the vibration response. This periodic "dip" every 0.1 s confirms the location of the fault relative to the blade passing sequence.

This phenomenon primarily arises from the sustained aerodynamic pressure acting on the blade surface, while the periodic passage of the upstream first-stage rotating blade induces a flow-blocking effect, leading to a transient reduction in local aerodynamic pressure and consequently causing synchronized sudden drops in the directional displacement. When blade fracture occurs in the upstream rotating blade, its flow-blocking capability is weakened, resulting in a reduced amplitude of aerodynamic pressure fluctuations and, accordingly, a significantly diminished magnitude of the displacement drops.

As shown in Figs. 3(b) and 4(b), the main characteristic frequency components in the model response are BPF and its harmonics, with the shaft rotational frequency amplitude significantly enhanced under fault conditions. Comparing the amplitude changes of key characteristic frequencies, the following conclusions are drawn:

(1) Blade fracture leads to an increase in the shaft rotational frequency amplitude in the response. Under normal conditions, no shaft rotational frequency amplitude is observed in the model spectrum; under fault conditions, the shaft rotational frequency amplitude is prominent, reaching 0.0609 μm.

(2) Blade fracture results in a decrease in the BPF amplitude in the response. Under normal conditions, the BPF amplitude is 2.3911 μm and the multiple BPF frequency amplitude is 1.0149 μm; under fault conditions, the BPF amplitude is 2.3433 μm and the multiple BPF frequency amplitude is 0.9946 μm.

III. FULL-ENGINE FAULT EXPERIMENT SETUP AND VERIFICATION

A. DESIGN OF FULL-ENGINE EXPERIMENT FOR BLADE FRACTURE FAULTS

In this study, full-scale engine tests of blade fracture faults are conducted on an aero-engine test bench to verify the conclusions of the proposed model. The aero-engine test bench is shown in Fig. 5.

Fig. 5. Aero-engine test bench.

The blade fracture fault simulation test is carried out on the first-stage blade of the aero-engine high-pressure compressor, as shown in Fig. 6.

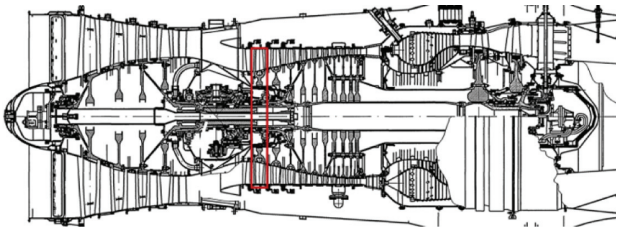

Fig. 6. Position of the high-pressure first-stage turbine blade used in the experiment.

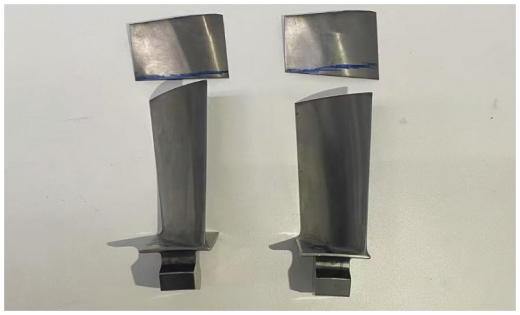

Fig. 7. Fractured rotor blade simulated by manual shearing.

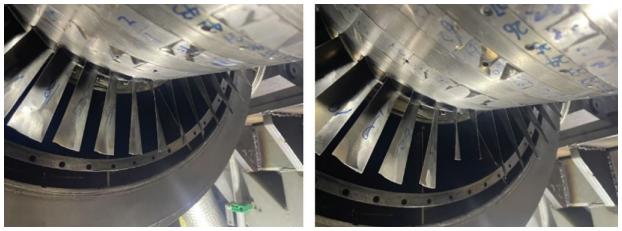

Fig. 8. Installed normal and fracture high-voltage first-stage blades.

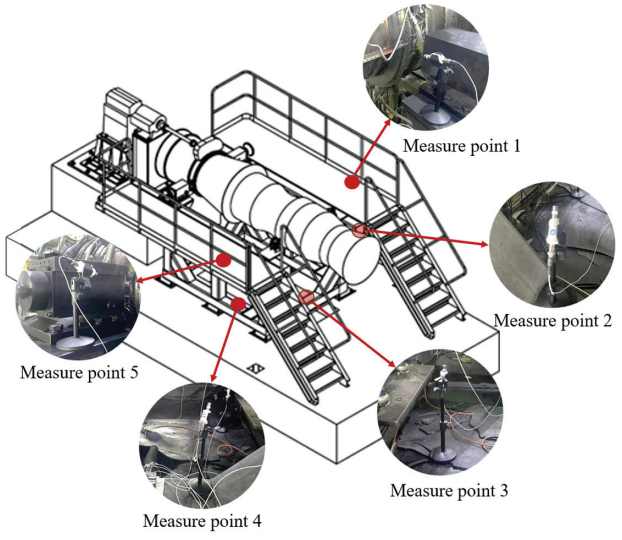

Fig. 9. Ring-shaped arrangement position of the noise sensor on the test bench.

In this study, a normal blade is processed by wire cutting to produce a fractured blade, as shown in Fig. 7. The normal blade is then replaced with the fractured blade and installed at the first-stage rotating blade of the high-pressure compressor in an aero-engine. The actual installation configuration is illustrated in Fig. 8.

B&K4519 accelerometers are used to collect vibration signals, and HT378A06 noise sensors are employed to acquire noise signals, with a sampling frequency of 51.2 kHz.

The accelerometers are mounted at the horizontal position of the front casing using bolted connections, and the noise sensors are arranged in a circular array. The arrangement of the noise sensors is illustrated in Fig. 9.

Tests are conducted under both normal and fault conditions, with synchronous collection of vibration and noise signals. Three main operating speeds of experiments are set: 4000 rpm, 5000 rpm, and 6000 rpm, with each speed maintained for 10 s to ensure stable operation.

B. ANALYSIS OF EXPERIMENTAL DATA FOR BLADE FRACTURE FAULTS

First, a comparative analysis of vibration signals under normal and blade fracture fault conditions is performed to validate the model predictions regarding the effects of blade fracture on shaft rotational frequency and BPF amplitudes.

The changes in shaft rotational frequency amplitude in the vibration signal spectrum are shown in Fig. 10, with detailed amplitude data summarized in Table I.

As illustrated in Fig. 10, the shaft rotational frequency remains the dominant component in the low-frequency

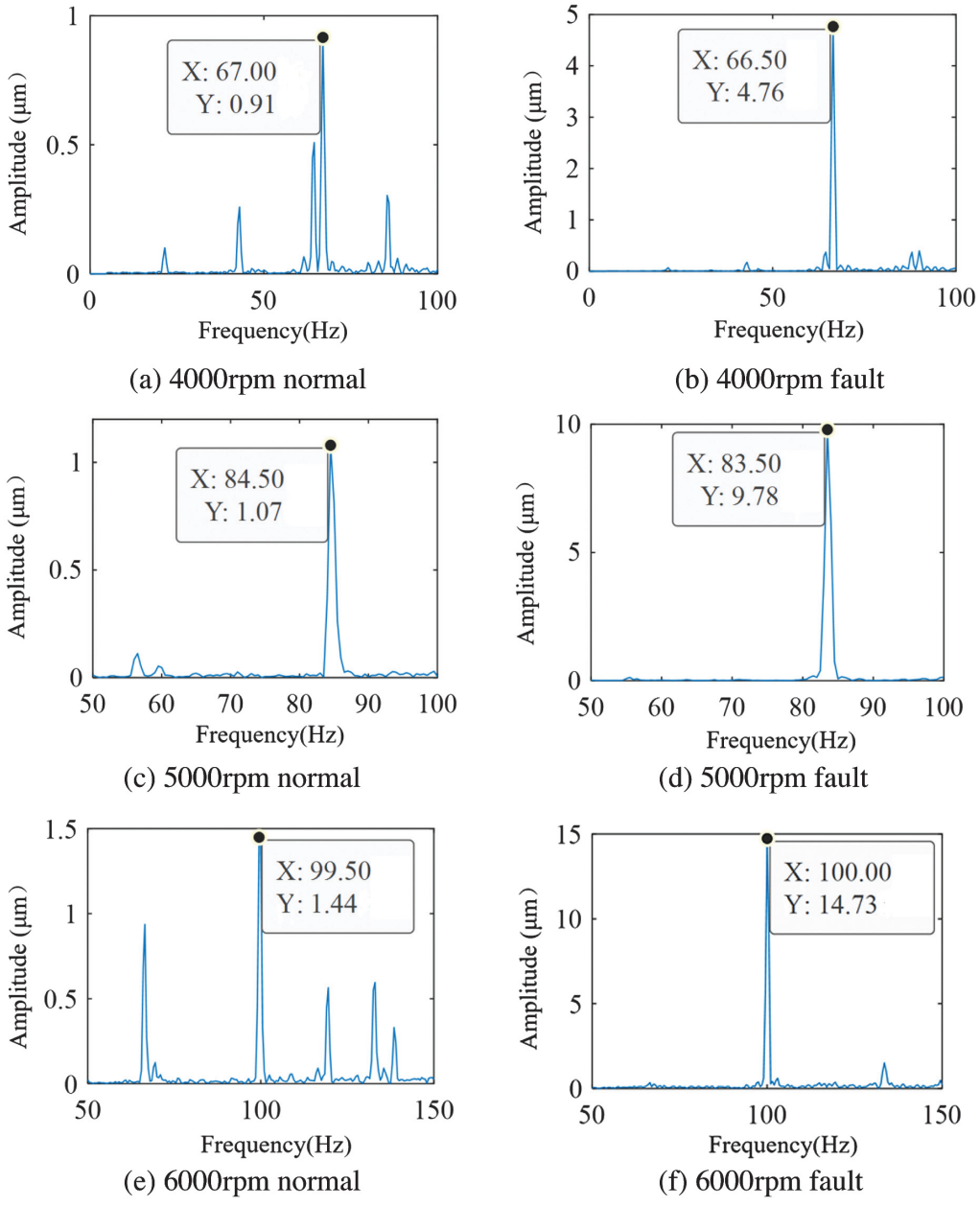

Fig. 10. Fundamental frequency spectrum variation plots of normal and fracture blade vibration data. (a) 4000 rpm normal. (b) 4000 rpm fault. (c) 5000 rpm normal. (d) 5000 rpm fault. (e) 6000 rpm normal. (f) 6000 rpm fault.

region of the system vibration spectrum under both normal and fault operating conditions.

Further analysis of the amplitudes summarized in Table I shows that the shaft rotational frequency amplitude of the vibration signal is significantly increased under fault conditions at all tested speeds (4000 rpm, 5000 rpm, and 6000 rpm). This conclusion is consistent with the model simulation results, validating the accuracy of the simulation.

Table I. Fundamental frequency amplitude variation list

Rotational speed (rpm)	Normal amplitude (μm)	Fault amplitude (μm)	Amplitude variation (μm)
4000	0.91	4.76	3.85
5000	1.07	9.78	8.71
6000	1.44	14.73	13.29

The changes in BPF amplitude in the vibration signal spectrum are shown in Fig. 11, with detailed amplitude data summarized in Table II.

As illustrated in Fig. 11, a pronounced BPF component is observed in the system vibration spectrum under both normal and fault conditions.

As shown in Table II, the BPF amplitude of the vibration signal is significantly reduced under fault conditions at all tested speeds. This conclusion is also consistent with the model simulation results.

Further analysis is conducted on the noise signals collected during the full-engine tests. Due to severe environmental interference on low-frequency components of noise signals, the analysis focuses on high-frequency data, specifically changes in BPF amplitude.

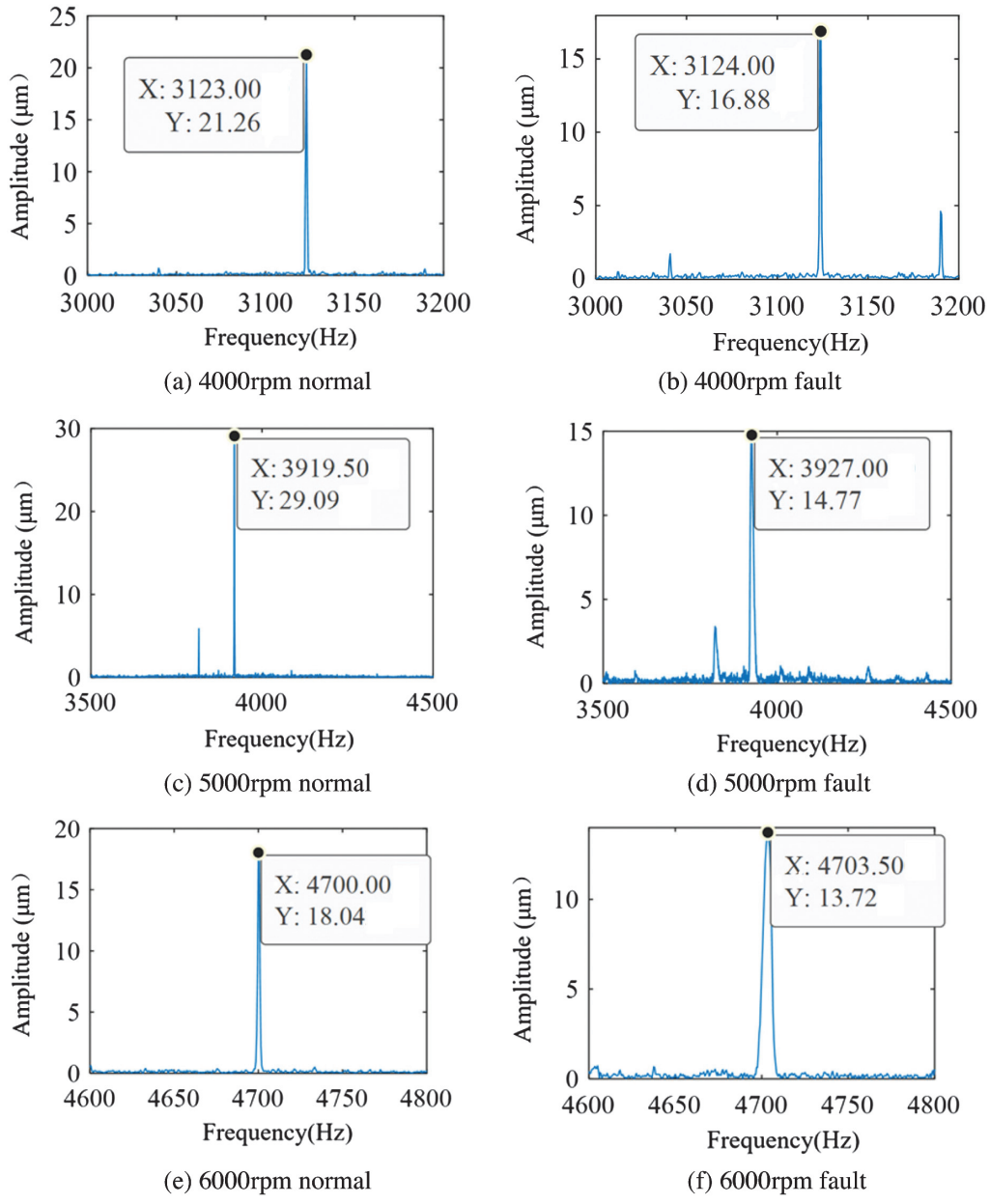

Fig. 11. BPF spectrum variation plots of normal and fracture blade vibration data. (a) 4000 rpm normal. (b) 4000 rpm fault. (c) 5000 rpm normal. (d) 5000 rpm fault. (e) 6000 rpm normal. (f) 6000 rpm fault.

Table II. Blade passing frequency (BPF) amplitude variation list

Rotational speed (rpm)	Normal amplitude (μm)	Fault amplitude (μm)	Amplitude variation (μm)
4000	21.26	16.88	4.38
5000	29.09	14.77	14.32
6000	18.04	13.72	4.32

Table III. Blade passing frequency (BPF) amplitude variation list

Rotational speed (rpm)	Normal amplitude (μm)	Fault amplitude (μm)	Amplitude variation (μm)
4000	8.27	4.28	3.99
5000	10.80	8.31	2.49
6000	22.05	16.11	5.94

The changes in BPF amplitude of the noise signal under normal and fault conditions are shown in Fig. 12, with detailed amplitude data summarized in Table III.

As illustrated in Fig. 12, a pronounced BPF component appears in the system noise response spectrum under both normal and fault conditions, showing good agreement with the vibration response.

As shown in Table III, the BPF amplitude of the noise signal is significantly reduced under fault conditions at all

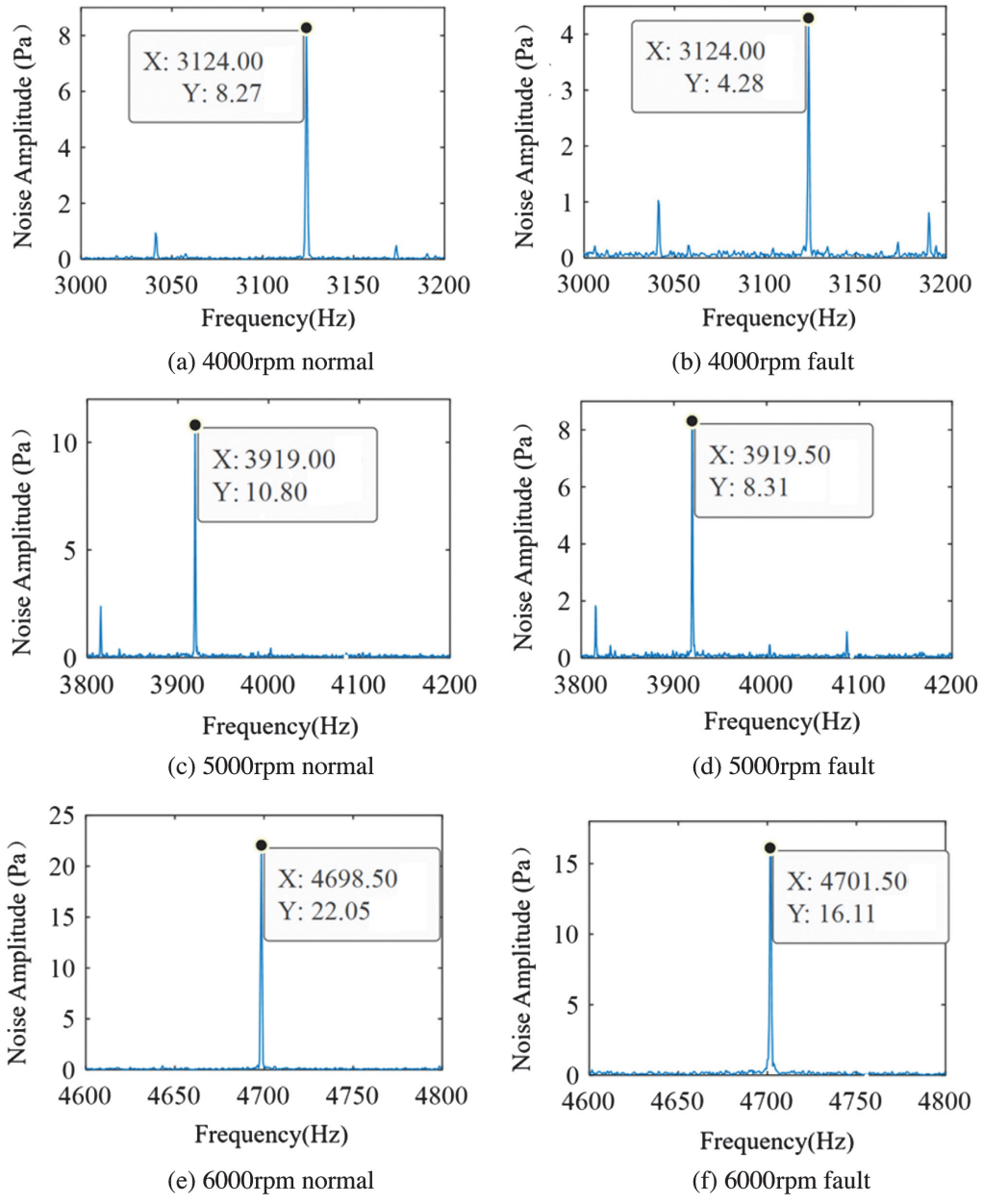

Fig. 12. BPF spectrum variation plots of normal and fractured blade noise data. (a) 4000 rpm normal. (b) 4000 rpm fault. (c) 5000 rpm normal. (d) 5000 rpm fault. (e) 6000 rpm normal. (f) 6000 rpm fault.

tested speeds. This variation trend is consistent with that of the vibration signal and the simulation analysis results.

IV. CONCLUSIONS

This study investigates the noise and vibration response characteristics of aero-engine blade fracture faults through a combination of numerical simulation and full-engine experiments. The main conclusions are as follows:

(1) A coupled model integrating stator blade dynamics and wake excitation force is constructed, which accurately reproduces the dynamic response law of blades in an aerodynamic environment, quantifies the influence of wake excitation force on system response, and reveals the mechanism by which blade fracture affects aerodynamic excitation.

(2) Both simulation and experimental results demonstrate that blade fracture faults lead to an increase in the shaft rotational frequency amplitude and a decrease in the BPF amplitude in vibration signals. The BPF amplitude in noise signals exhibits the same variation trend as that in vibration signals.

(3) The results of full-engine-level fault simulation tests are consistent with the predicted variation trends of fault characteristic frequencies and their amplitudes, effectively validating the accuracy and effectiveness of the proposed model. This provides a theoretical basis and engineering reference for blade fracture fault diagnosis under complex operating conditions.

CONFLICT OF INTEREST STATEMENT

The authors declare no conflicts of interest.

REFERENCES

[1] L.-H. Yang *et al.*, "Dynamic characteristic analysis of rotating blade with transverse crack—Part I: Modeling, modification, and validation," *J. Vib. Acoust.*, vol. 143, no. 5, pp. 1–36, 2021.

[2] L.-H. Yang *et al.*, "Dynamic coupling vibration of rotating shaft–disc–blade system — Modeling, mechanism analysis and numerical study," *Mech. Mach. Theory*, vol. 167, pp. 61–98, 2022.

[3] K. Feng *et al.*, "Gas turbine blade fracturing fault diagnosis based on broadband casing vibration," *Measurement*, vol. 214, 2023.

[4] P. A. A. Baracat and K. A. R. Ismail, "Ideal blade sweep model for horizontal axis wind turbines with different chord and twist distributions," *Wind Energy Eng. Res.*, vol. 4, 2025.

[5] I. Mahariq *et al.*, "Identification of nonlinear model for rotary high aspect ratio flexible blade using free vibration response," *Alex. Eng. J.*, vol. 59, no. 4, pp. 2131–2139, 2020.

[6] C. Wang *et al.*, "Model reduction and damping mistuning identification method for mistuned rotating bladed disks under variable speed," *J. Sound.Vib.*, vol. 619, 2025.

[7] A. S. M. Smyth, F. Zilic de Arcos, and A. M. Young, "Modelling unsteady hydrodynamic gust loading on tidal turbine blades," *J. Fluids Struct.*, vol. 137, 2025.

[8] B. He *et al.*, "Dynamic modeling and characteristics of integrally shrouded group blades with two-dimensional rub-impact considering the stick-slip motion," *Appl. Math. Model.*, vol. 148, 2025.

[9] J. Zhang *et al.*, "A weak fault identification method of microturbine blade based on sound pressure signal with LSTM networks," *Aerosp. Sci. Technol.*, vol. 136, 2023.

[10] C. Subramanian *et al.*, "Fatigue fracture of last stage X20Cr13 low pressure turbine (LPT) blade from 600 MW thermal power station," *Inter. J. Press. Vessels. Pip.*, vol. 221, 2026.

[11] W. Nie *et al.*, "Test rig and experimental Investigation on the blade containment of aero-engine turbine casing," *Eng. Fail. Anal.*, vol. 178, 2025.

[12] D. Wei *et al.*, "A novel method for vibration measurement of rotating blisk based on blade tip pulse width," *Measurement*, vol. 249, 2025.

[13] J. Du *et al.*, "Jet noise location and identification of aero-engine based on Clean-SC," *Gas Turbine Exp. Res.*, vol. 36, no. 3, pp. 25–29, 2023 (in Chinese).

[14] A. Kumar, "Research overview and prospect in condition monitoring of compressors," *Expert Syst. Appl.*, vol. 277, 2025.

[15] P. Hou *et al.*, "Comparative investigation of region-specific acoustic emission responses during artificial crack extension in a full-scale wind turbine blade," *Measurement*, vol. 264, 2026.

[16] F. Zhao *et al.*, "Experimental study of rotor blades vibration and noise in multistage high pressure compressor and their relevance," *Chin. J. Aeronaut.*, vol. 33, no. 3, pp. 870–878, 2020.

[17] M. Rafiee, F. Nitzsche, and M. Labrosse, "Dynamics, vibration and control of rotating composite beams and blades: A critical review," *Thin-Walled Struct.*, vol. 119, pp. 795–819, 2017.

[18] G.-J. Shen *et al.*, "Theoretical and experimental harmonic analysis of cracked blade vibration," *Measurement*, vol. 222, 2023.

[19] F. Wang *et al.*, "Experimental investigation of acoustic resonance in aero-engine compressors based on fluid–structure–acoustic multi-physics measurements," *Aerosp. Sci. Technol.*, vol. 174, 2026.

[20] P. Kundu, "Review of rotating machinery elements condition monitoring using acoustic emission signal," *Expert Syst. Appl.*, vol. 252, Part B, 2024.

[21] Z.-Y. Wu *et al.*, "Axial-bending coupling vibration characteristics of a rotating blade with breathing crack," *Mech. Syst. Signal Process.*, vol. 182, 2023.

[22] L. Hou *et al.*, "Inter-shaft bearing fault diagnosis based on aero-engine system: A benchmarking dataset study," *J. Dyn. Monit. Diagn.*, vol. 2, no. 4, pp. 228–242, 2023.

[23] Z.-Y. Wu *et al.*, "Influences of blade crack on the coupling characteristics in a bladed disk with elastic support," *Aerosp. Sci. Technol.*, vol. 133, 2023.

[24] Z.-Y. Wu *et al.*, "Modal characteristics of a flexible dual-rotor coupling system with blade crack," *J. Sound and Vib.*, vol. 567, 2023.

[25] Z.-Y. Wu *et al.*, "Vibration characteristics of a shaft–disk–cracked-blade coupling system under multisource excitation," *AIAA J.*, vol. 63, pp. 2954–2970, 2025.